

# A Portable Airborne Scanning Lidar System for Ocean and Coastal Applications

BENJAMIN D. REINEMAN

*Mechanical and Aerospace Engineering, and Scripps Institution of Oceanography,  
University of California, San Diego, La Jolla, California*

LUC LENAIN, DAVID CASTEL, AND W. KENDALL MELVILLE

*Scripps Institution of Oceanography, University of California, San Diego, La Jolla, California*

(Manuscript received 27 March 2009, in final form 26 June 2009)

## ABSTRACT

A portable compact airborne scanning lidar system based on the Riegl LMS-Q240i has been developed and its functionality demonstrated for oceanographic and coastal measurements. Differential GPS (DGPS) and an inertial navigation system are synchronized with the lidar, resulting in vertical rms errors of less than 9 cm. Surveys with this airborne system are compared with ground-based DGPS surveys of fixed targets. Measurements of the southern California coastline and nearshore surface wave fields from 17 research flights between August 2007 and December 2008 are analyzed and discussed. The October 2007 landslide on Mt. Soledad in La Jolla, California, was documented by two of the flights. The topography, lagoon, reef, and surrounding wave field of Lady Elliot Island in Australia's Great Barrier Reef were measured with the airborne scanning lidar system on eight research flights in April 2008. Applications of the system, including coastal topographic surveys, wave measurements, ship wake studies, and coral reef research, are presented and discussed.

## 1. Introduction

Airborne scanning light detection and ranging (lidar) is widely used as a mapping tool for a variety of applications. Coastal and nearshore ocean surveys in particular do not require the range or capability of larger aircraft, so there is an incentive to develop smaller, lighter, and cheaper lidar systems that can be used in small single- or twin-engine aircraft.

Spatiotemporal measurements of ocean wave fields have been made by Hwang et al. (2000), Melville et al. (2005), and Romero and Melville (2010a), using the Airborne Topographic Mapper (ATM), a conically scanning lidar developed by NASA and EG&G Technical Services. The latter two studies measured the evolution of the wave directional spectrum in fetch-limited conditions in the Gulf of Tehuantepec from a Lockheed C-130. The ATM has also been flown in Lockheed P-3 Orions and de Havilland Canada DHC-6 Twin Otters. The ATM uses

a class 4, 550-nm laser with a pulse repetition rate (PRR) of 5 kHz. Operating at an altitude of 400 m with a conical scan rate of 20 Hz and off-nadir angle of 15°, it has a point spacing of approximately 5 m along track and 2.5 m cross track (Romero and Melville 2010a). The vertical rms error of the ATM is estimated at 15 cm (Sallenger et al. 2003).

Coastal erosion due to seasonal wave and storm activity has been quantified in many studies with several different airborne lidar systems. Robertson et al. (2007) measured beach erosion caused by Hurricane Ivan using three systems: the Optech Airborne Laser Terrain Mapper (ALTM) 1233, NASA Experimental Advanced Airborne Research Lidar (EAARL), and Optech Scanning Hydrographic Operational Airborne Lidar Survey (SHOALS) 3000. The ALTM 1233 uses a 1100-nm laser and has a PRR of 33 kHz. The EAARL uses two lasers, both pulsed at 3 kHz: a 532-nm laser for bathymetric surveying to 30-m depth in clear water and a 1064-nm laser for topography. The SHOALS-3000 system uses a 532-nm laser for bathymetric surveying to 50-m depth in very clear water, pulsed at 3 kHz, and a 1064-nm laser for topography, pulsed at 20 kHz. The ATM has also been used for beach erosion studies by Brock et al. (2002), Woolard and Colby (2002), Sallenger et al. (2002),

---

*Corresponding author address:* Benjamin D. Reineman, University of California, San Diego, 9500 Gilman Dr., La Jolla, CA 92093-0213.  
E-mail: reineman@ucsd.edu

Report Documentation Page				Form Approved OMB No. 0704-0188	
Public reporting burden for the collection of information is estimated to average 1 hour per response, including the time for reviewing instructions, searching existing data sources, gathering and maintaining the data needed, and completing and reviewing the collection of information. Send comments regarding this burden estimate or any other aspect of this collection of information, including suggestions for reducing this burden, to Washington Headquarters Services, Directorate for Information Operations and Reports, 1215 Jefferson Davis Highway, Suite 1204, Arlington VA 22202-4302. Respondents should be aware that notwithstanding any other provision of law, no person shall be subject to a penalty for failing to comply with a collection of information if it does not display a currently valid OMB control number.					
1. REPORT DATE <b>2009</b>		2. REPORT TYPE		3. DATES COVERED <b>00-00-2009 to 00-00-2009</b>	
4. TITLE AND SUBTITLE <b>A Portable Airborne Scanning Lidar System for Ocean and Coastal Applications</b>				5a. CONTRACT NUMBER	
				5b. GRANT NUMBER	
				5c. PROGRAM ELEMENT NUMBER	
6. AUTHOR(S)				5d. PROJECT NUMBER	
				5e. TASK NUMBER	
				5f. WORK UNIT NUMBER	
7. PERFORMING ORGANIZATION NAME(S) AND ADDRESS(ES) <b>Mechanical and Aerospace Engineering, and Scripps Institution of Oceanography, University of California, San Diego, LaJolla, CA</b>				8. PERFORMING ORGANIZATION REPORT NUMBER	
9. SPONSORING/MONITORING AGENCY NAME(S) AND ADDRESS(ES)				10. SPONSOR/MONITOR'S ACRONYM(S)	
				11. SPONSOR/MONITOR'S REPORT NUMBER(S)	
12. DISTRIBUTION/AVAILABILITY STATEMENT <b>Approved for public release; distribution unlimited</b>					
13. SUPPLEMENTARY NOTES					
14. ABSTRACT					
15. SUBJECT TERMS					
16. SECURITY CLASSIFICATION OF:			17. LIMITATION OF ABSTRACT <b>Same as Report (SAR)</b>	18. NUMBER OF PAGES <b>17</b>	19a. NAME OF RESPONSIBLE PERSON
a. REPORT <b>unclassified</b>	b. ABSTRACT <b>unclassified</b>	c. THIS PAGE <b>unclassified</b>			

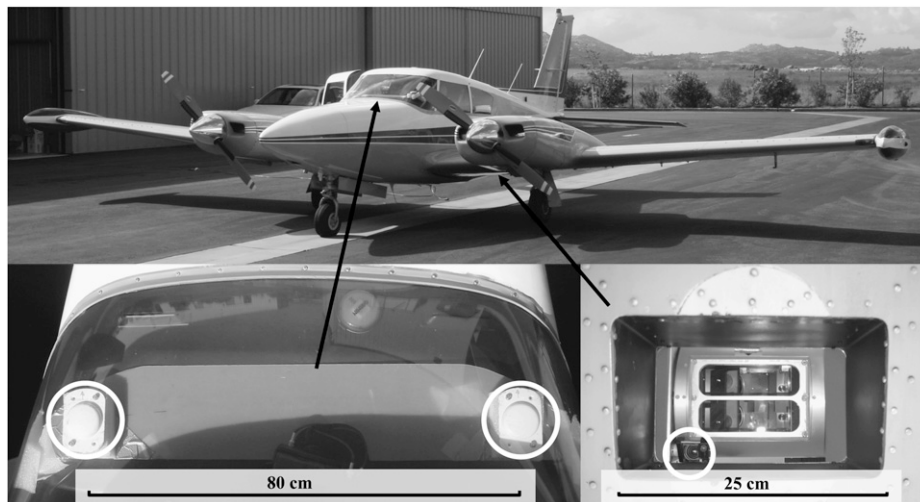


FIG. 1. Piper Twin Comanche, used for southern California surveys: (bottom left) the GPS antennas on the dashboard (circled) and (bottom right) view looking up through the rectangular hole in the floor of the aircraft. The mirror for the 3CCD camera is circled.

Stockdon et al. (2002), Sallenger et al. (2003, 2006), and Young and Ashford (2006). These fully integrated systems are expensive to purchase and operate, and missions may require planning months in advance, especially when using larger, less available aircraft. In addition, they use class 4 lasers, which have minimum flight altitude requirements over populated areas.

An Optech ALTM 1225, installed in a Cessna 206 or Partenavia P-68 Observer, has been used to survey southern California beaches semiannually since 2002 (Yates et al. 2008). The ALTM 1225 uses a class 4, 1024-nm laser, pulsed at 25 kHz, which has a minimum eye-safe flight altitude of 300 m. Airborne surveys are planned months in advance, and in situ GPS surveys must be used to resolve changes in beach morphology due to single storm events (Yates 2009).

With the development of lighter and cheaper commercial lidar and GPS/inertial navigation systems (INS), a larger range of scientific and technical problems can be addressed using smaller aircraft that have sufficient capability while being less expensive to operate. For example, Forsberg et al. (2001) developed a lidar system based on a Riegl LMS-Q140i. The Q140i uses a 904-nm class 1 (eye safe) scanning laser with a PRR of 30 kHz. It has been used for ice elevation studies in Greenland and Patagonia in Twin Otters (Forsberg et al. 2001; Keller et al. 2007). With a Honeywell H-764G INS, a Trimble 4000SSI, and Javad Legacy GPS receivers, the system has an estimated vertical accuracy of 15 cm in tests near a GPS base station (<50 km) and 30 cm in surveys up to 100 km from base stations.

In this paper, we describe the performance and application of an airborne lidar system based on the Riegl

LMS-Q240i scanning lidar and the CodaOctopus F180+ GPS/INS for coastal and oceanographic research—fields historically explored with larger, more expensive systems. The Q240i has a PRR of 30 kHz and has a class 1 laser safety rating, which allows the system to be flown at low altitude, often below cloud ceiling. A light, twin-engine, four-passenger Piper Twin Comanche (Fig. 1) was used for flights in southern California. A Cessna Caravan was used for flights over Australia's Great Barrier Reef (GBR).

In section 2, we describe the system instrumentation and operation, data processing, and calibration. In section 3, we discuss the system performance and validation. In section 4, we present coastal and oceanographic applications that we have explored with flights in southern California and over Lady Elliot Island (LEI; <http://www.ladyelliot.com.au/>) in the GBR.

## 2. System description

The airborne scanning lidar system presented here was designed for cost effectiveness and portability. Total instrumentation cost is a small fraction of the cost of a turnkey fully integrated commercial system.

### a. Instrumentation and synchronization

The airborne lidar system is shown in Fig. 2. The lidar is the Riegl LMS-Q240i, which uses a 905-nm laser that is class 1 (eye safe) while scanning: safety circuits ensure that it is always scanning while the laser is active. The beam has a 2.7-mrad divergence and is directed by a rotating polygonal mirror along lateral swaths at a specified rate, with an 80° field of view (geometrically

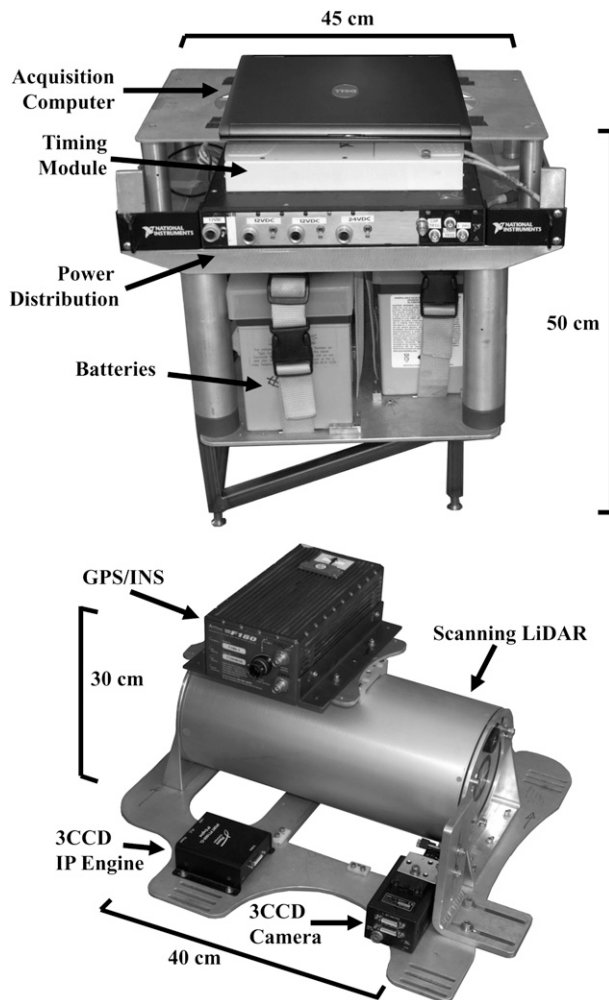


FIG. 2. Airborne lidar instrumentation: (top) the power and data acquisition rack and (bottom) the scanning lidar, GPS/INS, and 3CCD camera.

limited to  $50^\circ$  in the Twin Comanche owing to the size of the nadir-looking port and the distance between the cabin floor and the outer skin of the aircraft). Range is measured by time of flight. An 8-bit measure of the returned pulse signal strength is also recorded for each point. The laser has a pulse repetition rate of 30 kHz, and the angle increment between pulses  $\Delta\theta$  is set to  $0.24^\circ$ , which gives a swath repetition rate of 30 Hz.

A CodaOctopus F180+ dual-antennae GPS/INS provides position and attitude information. The unit, which uses Novatel OEM4 receivers and has been upgraded to be L1/L2 capable on both antennae, is rigidly mounted to the lidar. Low profile antennae are configured on the aircraft dashboard underneath the acrylic windshield, with a baseline (distance between the two antennae) of 79 cm in the Comanche and 103 cm in the Caravan. This is convenient for a portable system as described here.

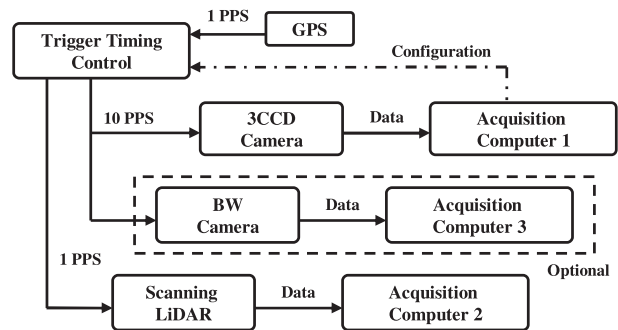


FIG. 3. Airborne lidar system flowchart. The lidar internal clock is slaved to GPS at 1 PPS. The black-and-white 11-megapixel camera is optional.

For frequent use in the same aircraft, permanent installation of GPS antennae on the exterior of the fuselage could increase the antennae baseline and increase the number of satellites in view, thereby providing small improvements to position and heading accuracy. Differential GPS (DGPS) is processed postflight with base station data (see section 2c).

A  $3 \times 1$  megapixel JAI CV-M9CL 8/10-bit, 3-charge-coupled device (3CCD) camera mounted beside the lidar is triggered at 10 Hz. For LEI/GBR flights, we added an 11-megapixel ImperX IPX-11M5-G 12-bit black and white camera, also triggered at 10 Hz.

Instrumentation synchronization is controlled with a National Instruments NI-6251 USB data acquisition board (DAQ). The single pulse per second (PPS) provided by the GPS resets the internal lidar clock, which has negligible drift over one second. The 10 PPS for the camera(s) is also phase locked to the GPS 1 PPS (Fig. 3).

Independently powered laptops record the data. The lidar streams approximately 5.8 MB of data per minute; the 3CCD camera approximately  $1.4 \text{ GB min}^{-1}$ ; and the GPS/INS, which is self-logging, records at approximately  $0.5 \text{ MB min}^{-1}$ .

The combination of self-contained power and the dashboard-mountable antennae makes the system portable and platform independent, given a suitable nadir-looking port in the aircraft.<sup>1</sup> The class 1 laser rating allows the system to be flown at low altitudes, often below cloud ceiling, increasing point density per pass and decreasing attitude-induced errors (see section 2d). This low-altitude capability is particularly important in coastal applications, where marine layers may limit the use of lidar systems that are restricted to higher altitudes.

<sup>1</sup> In the absence of a nadir-looking port, in some past tests we have used a modified luggage door on the side of the fuselage of a Cessna 172 and  $45^\circ$  mirrors to provide nadir optical access.

### b. System setup and operation

The design also allows for a quick response and set-up time. From start of system installation to flight-ready status takes approximately 1.5 h. For southern California surveys, the system is installed in a four-passenger Piper Twin Comanche (Fig. 1). A rear seat is removed and the power and data acquisition rack installed in its place. The cover for the nadir-looking port is removed, and the lidar and GPS/INS system is bolted to the cabin floor over a thin (5 mm) rubber sheet to absorb vibration. Data and power cables are connected, and the plane is positioned under open sky to initiate GPS satellite lock.

A mirror placed on the ground below the observation port at 45° is used for lidar and camera testing and for rough alignment of the camera field of view within the lidar field of view. Precise relative orientation of the lidar and camera(s) is determined in postprocessing, using identifiable benchmarks.

Once there is sufficient motion (e.g., while taxiing), the GPS/INS begins a self-calibration routine to determine the precise position of the INS relative to the GPS antennae using position measured by the GPS and the integrated position estimate from the INS. The process usually takes less than 20 min. The end result is applied in postprocessing to the complete flight.

Beach survey times are planned to coincide with low tides and high GPS satellite coverage. Weather maps from the National Weather Service (available online at <http://www.nws.noaa.gov/>) are examined prior to takeoff to verify that there are no adverse atmospheric conditions.

In addition to the pilot, only one observer/operator is required to conduct the flights. For coastal flights, the pilot flies by visual flight rules (VFR). Lidar data are displayed graphically in real time for the operator, and position over the desired targets is maintained through constant communication between operator and pilot.

Setup and flights aboard the Cessna Caravan in the GBR were similar to those in the Twin Comanche, with a few notable differences. The larger aircraft allowed for one or two extra observers/operators. For this experiment, three seats in the Caravan were removed for instrumentation. A larger nadir-looking port allowed access for a second camera, the ImperX IPX. The flight pattern over LEI consisted of parallel passes at altitudes between 110 and 130 m, spaced 125 m apart. Pass endpoints were preprogrammed into the aircraft navigation system, and the pattern was flown by two pilots for safety and navigation accuracy.

### c. Data processing

A series of postflight operations, summarized in Fig. 4, converts the lidar data into an earth reference frame.

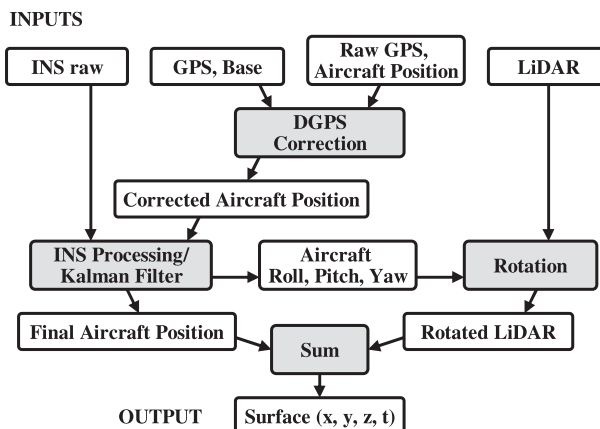


FIG. 4. Postprocessing flowchart for the airborne lidar system. Processes are shown in shaded boxes. The inputs are raw INS data, GPS positioning from the aircraft and the base stations, and the lidar range and scan angle information. After calibration and processing, we obtain georeferenced points in earth coordinates (see sections 2c and 2d).

Forward and reverse kinematic DGPS processing is completed using GPS base station data (see Brock et al. 2002) obtained, for southern California, from the Scripps Orbit and Permanent Array Center (available online at <http://sopac.ucsd.edu/>) and the UNAVCO archive (available online at <http://www.unavco.org/>). Coastal flights are typically less than 25 km from the nearest base station. At Lady Elliot Island, where publicly maintained GPS base stations are too distant (>90 km; available online at <http://www.ga.gov.au/geodesy/>), we deployed two Leica Geosystems GPS System 500 receivers (L1/L2 capable) sampling at 10 Hz as base stations near the runway. Surrounding wave field measurements were made typically less than 5 km from the base stations, with some flights ranging up to 30 km.

A 24-state Kalman filter routine processes the GPS/INS data and provides position and attitude [roll ( $\phi$ ), pitch ( $\alpha$ ), and heading ( $\psi$ )] data at 100 Hz (see Mohamed and Schwarz 1999). Position and attitude data are re-sampled by linear interpolation to the time of each lidar pulse. The range data from the lidar are rotated in three dimensions using the resampled roll, pitch, and heading and then added to the plane's instantaneous position, bringing the data into earth coordinates. The resulting "point cloud" can be interpolated to a fixed grid size for analysis.

Novatel's Waypoint GrafNav is used for DGPS corrections, and software from Oxford Technical Solutions is used for GPS/INS filtering and correction. Synchronization, rotation, and calibration are performed using The Mathworks' MATLAB, and the georeferenced point cloud is visualized with Applied Imagery's Quick Terrain Modeler.



#### d. Calibration and attitude errors

Consideration of the differences between the attitude reported by the INS and the actual attitude of the lidar reference frame is important in reducing georeferenced point positioning errors. Previous studies have provided in-depth explanations of the errors associated with lidar/INS alignment and calibration techniques to minimize these errors (Schenk 2001; Katzenbeisser 2003; Skaland and Lichti 2006). Here we take a simple, iterative approach to reduce the errors.

The attitude errors [roll ( $\phi_e$ ), pitch ( $\alpha_e$ ), and heading ( $\psi_e$ )] can be decomposed into the sum of the mean and fluctuating errors:

$$\phi_e = \overline{\phi_e} + \phi'_e, \quad (1)$$

where  $\overline{\phi'_e} = 0$ . The mean errors ( $\overline{\phi_e}$ ,  $\overline{\alpha_e}$ ,  $\overline{\psi_e}$ ) are the static alignment offsets between the lidar and the INS, and the time-varying fluctuating errors ( $\phi'_e$ ,  $\alpha'_e$ ,  $\psi'_e$ ) are mainly the result of sensor noise and random errors. To determine static roll offset ( $\overline{\phi_e}$ ), overlapping elevation maps from passes in opposing flight directions over an airport runway are compared. The average angle between the two elevation maps along the axis of the flight direction is calculated. Half of this angle is taken to be the static roll offset and is incorporated into the georeferencing algorithm, and new elevation maps are generated. The process is repeated until differences between the two map elevations are within the noise. A simplified version of the method presented by Filin (2003), using opposing flights over steep and variable terrain (unvegetated cliff faces), is used to estimate the pitch and heading offsets ( $\overline{\alpha_e}$ ,  $\overline{\psi_e}$ ), treating them as independent of the roll offset.

Surface position errors induced by attitude errors are not negligible. Attitude noise standard deviations are estimated by the Kalman filter and are typically  $0.03^\circ$  for roll ( $\phi_e$ ) and pitch ( $\alpha_e$ ) and  $0.10^\circ$  for heading ( $\psi_e$ ).

Assuming a flat surface and small angular errors, treating the errors as independent, and correcting for static offset errors in the georeferencing rotations, we can estimate vertical and horizontal errors due to time-varying attitude errors. These errors are a function of the swath angle  $\theta$  (the angle between vertical and the laser pulse direction, a maximum of  $25^\circ$  for the Comanche at level flight) and scale linearly with distance above the surface  $h$ .

Vertical roll errors vary as  $z_{e,\phi} = h \phi'_e \tan \theta$ . If we consider  $h = 170$  m and  $\phi'_e = 0.03^\circ$ , there will be a vertical error of 4.2 cm at swath extremes. Horizontal errors due to roll and pitch errors of  $0.03^\circ$  are less than 9 cm ( $x_{e,\phi} = h \phi'_e$ ;  $x_{e,\alpha} = h \alpha'_e$ ). Horizontal errors for a heading error of

$0.10^\circ$  are up to 14 cm at the swath extremes ( $x_{e,\psi} = h \psi'_e \tan \theta$ ). Measured vertical and horizontal errors are presented in section 3b.

### 3. Performance and validation

#### a. System performance

Point density is an important metric of system performance. We treat the 2D point density  $d$  as the product of along- and cross-flight densities:  $d = d_a d_c$ , where the along-flight density  $d_a$  is a function only of swath repetition rate (SRR) and aircraft speed  $v_0$ :  $d_a = \text{SRR } v_0^{-1}$ ; SRR is an adjustable parameter of the lidar unit, typically set to 30 Hz, so that, flying at  $66 \text{ m s}^{-1}$ , the along-flight point density is  $d_a = 0.45 \text{ m}^{-1}$ .

Cross-flight point density  $d_c$  is a function of the swath increment angle ( $\Delta\theta$ ), the target range and reflectivity, and the grazing angle of the laser pulses. By geometry, if all points are returned, the cross-flight point density for level flight is

$$d_c(x, h) = \frac{1}{\Delta x} = \frac{1}{h \Delta \theta} \left[ \frac{1}{1 + (x/h)^2} \right], \quad (2)$$

where  $x$  is the cross-swath distance from the centerline;  $h$  is height above the surface;  $\Delta x(x, h)$  is the cross-flight spacing between points; and  $\Delta \theta$  ( $\propto \text{SRR}^{-1}$ ) is the fixed angular scan increment, set to  $0.24^\circ$ . This profile is indicated by the dashed lines in Fig. 5.

The actual point density is estimated by examining airborne lidar data within a specified altitude range. The effects of aircraft motion are removed, and the density of points across the swath is calculated by averaging over multiple swaths. Sample measurements of point density at specified altitudes over land and ocean are shown in Fig. 5. Land targets are a mixture of vegetation and residential structures. Ocean data were collected on a calm day, with winds of  $2.6 \text{ m s}^{-1}$  and a significant wave height ( $H_s$ ) of 1.5 m. Wind speed was measured by National Data Buoy Center (NDBC) Station LJPC1 (available online at <http://www.ndbc.noaa.gov/>) and  $H_s$  by the Coastal Data Information Program (CDIP) Station 100 (available online at <http://cdip.ucsd.edu/>).

Density data are smoothed so that a “swath width” can be defined based on a specified density cutoff. Swath width as a function of altitude for various density cutoffs is shown in Figs. 6a and 6c, and average point density within the defined swath width in Figs. 6b and 6d.

Actual point density depends on surface reflectivity and the target angle relative to the laser pulse. The ocean surface is significantly less reflective than the mixed vegetation and structures over land, so there are fewer

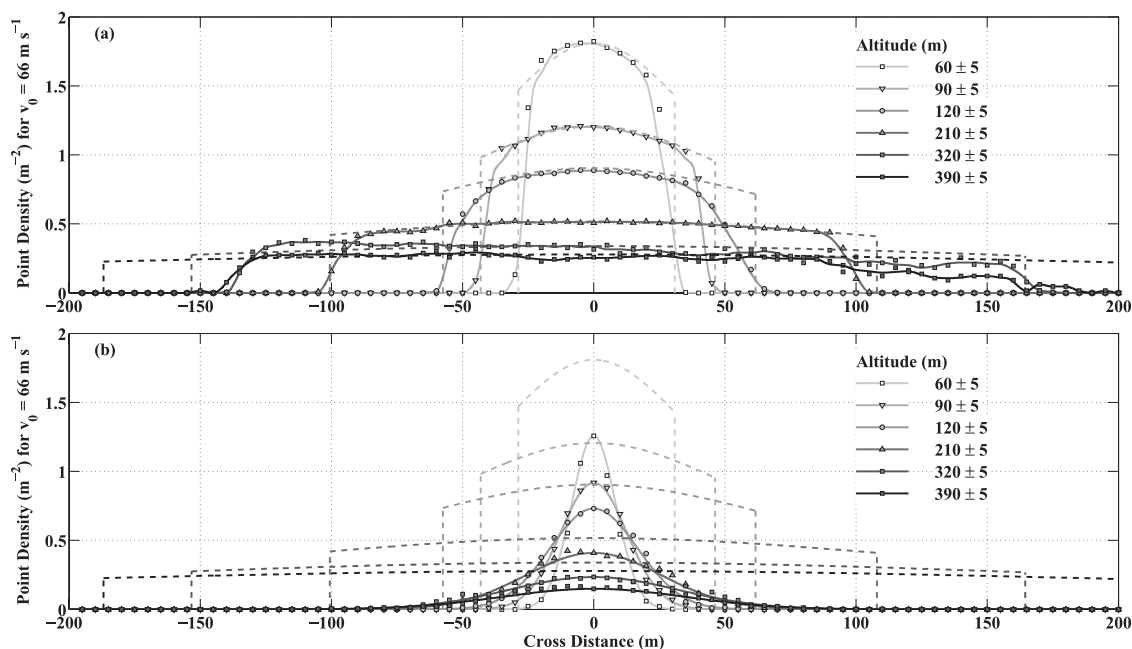


FIG. 5. 2D point density as a function of cross-swath distance as described in section 3a. (a) Data over land on an approach to the Ramona Airport runway, where targets are varied, including vegetation and residential structures. Measurements were taken during a 131-s descent from 390 to 60 m. (b) Data over the ocean during low wind and wave conditions (wind speed =  $2.6 \text{ m s}^{-1}$ ,  $H_s = 1.5 \text{ m}$ ). Measurements were taken during an 83-s descent from 390 to 60 m. Dashed lines show the theoretical maxima, based on geometry, if every laser pulse is returned. The smoothed connecting lines are generated so that a swath width can be determined for a given density cutoff (see Fig. 6).

returns and a lower point density over the ocean. From the dataset described above, the swath width is a maximum over land at approximately 360-m altitude and over the ocean on a calm day at around 240 m; higher altitude flights produce a narrower, less dense dataset. Flying 170 m above the surface, we achieve an average point density from  $0.3$  to  $0.5 \text{ m}^{-2}$  over the ocean and  $0.6$  to  $0.7 \text{ m}^{-2}$  over land with swath widths of 60–120 m over the ocean and 170 m over land.

### b. System validation

The vertical rms error of the complete system is calculated by comparing repeat passes over fixed targets. The runway of the Ramona Airport (KRNM), where the Comanche is based, is one such target, chosen because of convenience and GPS base station proximity. We linearly interpolate airborne lidar data from each pass over the runway to a common  $1200 \text{ m} \times 24 \text{ m}$  grid (the rectangular area in Fig. 7) with a grid spacing of 1 m in each direction to generate a mean elevation map.

The rms deviation from the mean elevation based on 17 passes from six days is 8.7 cm. Elevation data depend only on the airborne lidar system and the GPS base station, located less than 1 km from the runway, and have not been adjusted to match local benchmarks.

Ground transect surveys measured with the system GPS/INS as the aircraft taxis down the runway (dashed red line in Fig. 7) are in good agreement (9–11-cm rms difference) with the airborne lidar surveys. For this comparison, the interpolated lidar elevation for each pass is taken from the  $1 \text{ m} \times 1 \text{ m}$  grid box that contains each ground survey point.

Analyses of the lidar data from repeat passes over piers, helicopter landing pads, and other hard targets give similar results. Comparison with manual GPS surveys of an exposed coral reef gives rms differences of less than 10 cm, as discussed in section 4c.

Horizontal error is estimated by quantifying the relative alignment of georeferenced point clouds of varied topography from multiple airborne lidar passes. We selected 20 areas over varied cliff terrain, each approximately  $70 \text{ m} \times 70 \text{ m}$  and having at least 10 passes from two days. Mean elevation maps are created for each area, and the magnitude of the horizontal shift required to minimize vertical rms difference from the mean for each pass is calculated. We do not adjust lidar data to match local benchmarks. For 268 passes at altitudes of approximately 300 m, the horizontal error ranges from 0.02 to 1.47 m, with a rms value of 0.42 m. A histogram of these errors is shown in Fig. 8. This error is comparable to the

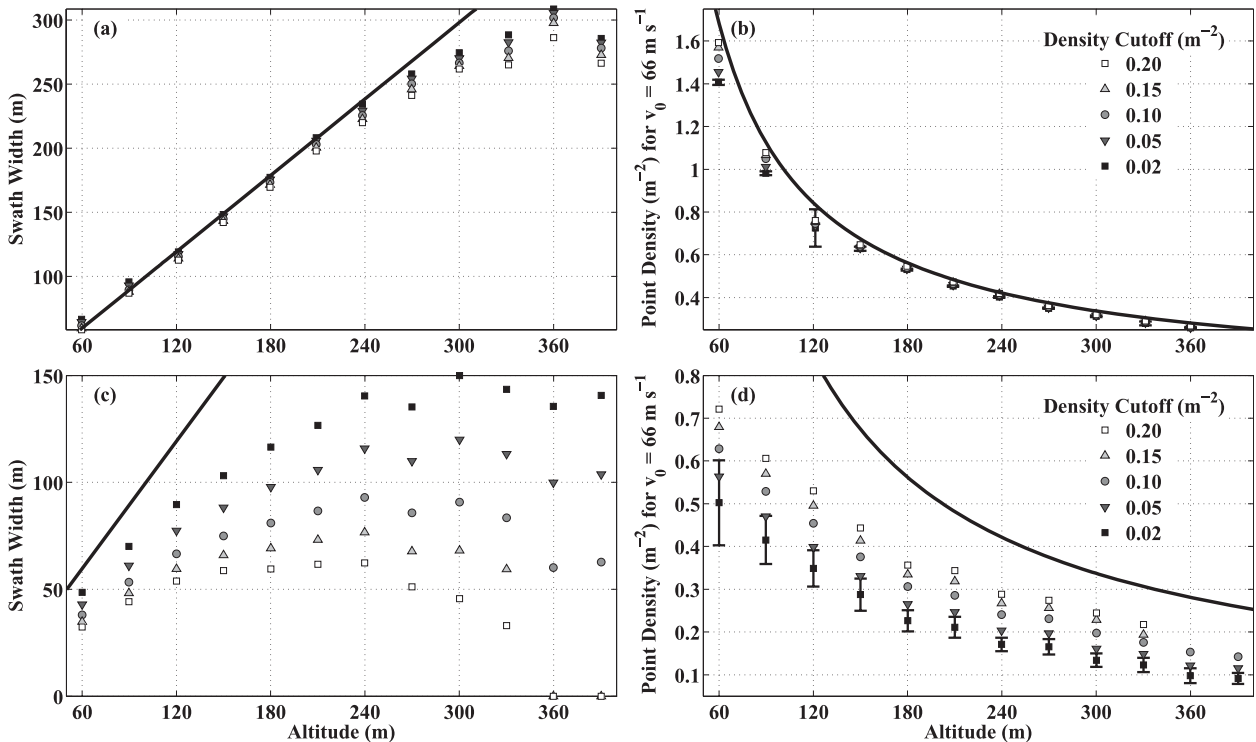


FIG. 6. (a),(c) Swath width and (b),(d) 2D point density as a function of height above the target. The dataset used is that in Fig. 5: (a),(b) from data over land and (c),(d) from data over the ocean. The solid black line is the geometric maximum, if every laser pulse is returned. Error bars in (b),(d) show one standard deviation from the mean for a density cutoff of  $0.02 \text{ m}^{-2}$ . Errors are similar for all density cutoffs considered.

estimated 0.80-m horizontal accuracy of the NASA ATM flown at an altitude of 700 m (Meredith et al. 1999).

## 4. Applications

### a. Beach morphology and erosion

Three surveys of the same segment of beach in Camp Pendleton Marine Corps Base, California, were conducted to measure the effect of several moderate storm events (Fig. 9). Significant wave height ( $H_s$ ) for November and December 2008, measured by CDIP station 043, located 2.7 km offshore of the southern end of the survey site, is shown in Fig. 9a. Water level, measured at the NOAA National Ocean Service Station 9410230 (available online at <http://tidesandcurrents.noaa.gov/>), located 45 km south of the survey area, is shown in Fig. 9b.

For each day, multiple passes ( $\geq 5$ ) at altitudes of 300–350 m gave point densities of approximately  $1.5 \text{ m}^{-2}$  over the survey area. The combination of an elevation cutoff and a cutoff based on the identification of interpass variability is used to detect and eliminate laser returns over the water. This method is similar to that used by Stockdon et al. (2002) and attempts to isolate the exposed beach. More advanced methods for water return

detection (see Yates et al. 2008) more precisely account for breaking wave setup and wave runup but are not included in this analysis.

The beach had reached a moderately accreted equilibrium state before the first survey and the subsequent storm event so that significant erosion of the exposed beach was measured between the first and second surveys (Fig. 9c). Also notable in this particular beach segment is the alongshore variability in erosion and accretion between surveys (Figs. 9c and 9d), showing a dominant pattern with an approximate spacing of 400 m.

The low cost of our system, flown in a light twin-engine aircraft, makes relatively frequent airborne measurements of beach topography possible. Thus, we are able to capture both episodic erosion caused by large storm events and the more gradual beach accretion phases. The high spatial density and timely response achievable with this airborne lidar system could aid in refining wave erosion models (M. L. Yates 2009, personal communication).

### b. Ocean waves

We conducted flights in the Santa Barbara Channel (in the Southern California Bight) in conjunction with the Office of Naval Research's (ONR) Radiance in a



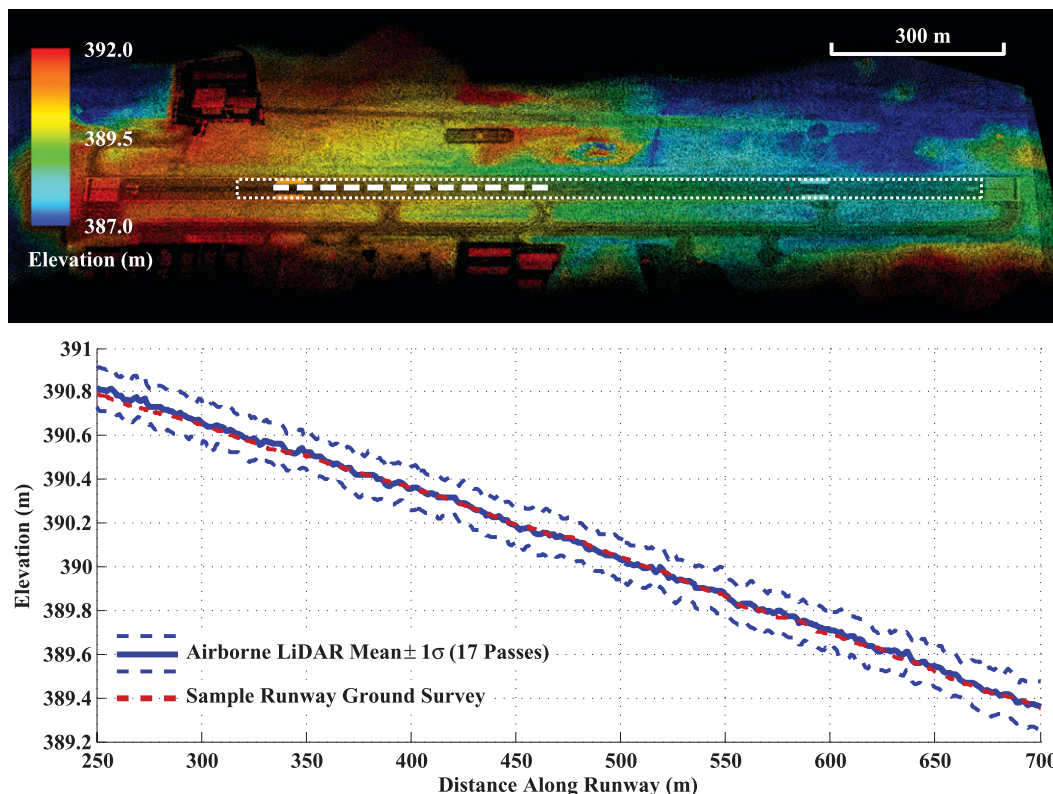


FIG. 7. Repeat lidar measurements over the runway of the Ramona Airport (KRNM; 33.039°N, 116.915°W). Elevation is shown in color, with shading indicating lidar backscattered amplitude (darkest being least reflective). The dotted rectangle shows the area over which vertical rms error is calculated (see section 3b). The mean and standard deviation of the elevation of the section marked by the dashed white line (top panel) are shown in blue (bottom panel). The dashed red line shows a sample ground survey over the same section.

Dynamic Ocean (RaDyO) experiment in September 2008. Simultaneous wave and meteorological data comes from instruments aboard the Scripps Institution of Oceanography R/P *FLIP*. Figure 10 shows a sample omnidirectional wave spectrum calculated from a  $10 \text{ km} \times 80 \text{ m}$  section of airborne lidar data. Mean wind speed 10 m above the surface at the survey time as measured on *FLIP* was  $U_{10} = 8.7 \text{ m s}^{-1}$ . Low-altitude (120 m) upwind flights allowed a ground speed of  $53 \text{ m s}^{-1}$  and gave point densities from  $1.1 \text{ m}^{-2}$  at the center of the swath to  $0.3 \text{ m}^{-2}$  at the edges. The Doppler shift due to aircraft motion is accounted for in the analysis (see Walsh et al. 1985; Hwang et al. 2000). Measurements are linearly interpolated to a  $1 \text{ m} \times 1 \text{ m}$  grid, and a Hanning window is used to taper the edges in along- and cross-flight orientations (see Romero and Melville 2010a).

The system is able to clearly resolve the omnidirectional equilibrium spectra varying as  $k^{-5/2}$ , as predicted by Phillips (1985), assuming a balance of wind input, dissipation, and nonlinear interactions. This spectral slope has also been observed by Hwang et al. (2000) and Romero and Melville 2010a and numerically reproduced by

Onorato et al. (2002), Dysthe et al. (2003), Badulin et al. (2005), and Romero and Melville (2010b). At higher wavenumbers ( $k > 0.35 \text{ rad m}^{-1}$ ), the saturation spectrum  $k^{-3}$  is visible.

We have also tested the ability of our system to measure ship wakes with several arranged passes on 10 July 2008 over the Catalina Jet Cat Express, a 44-m catamaran

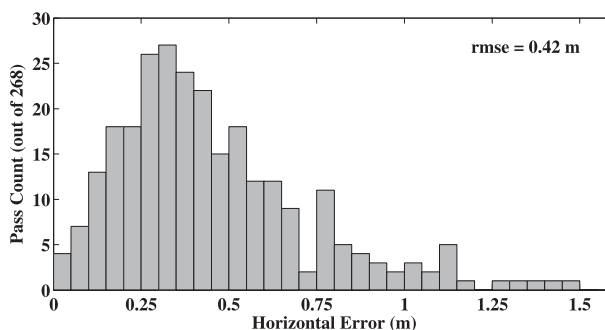


FIG. 8. Histogram of horizontal errors in lidar data taken from an altitude of 300 m. The rms error is 0.42 m. The calculation is described in section 3b.

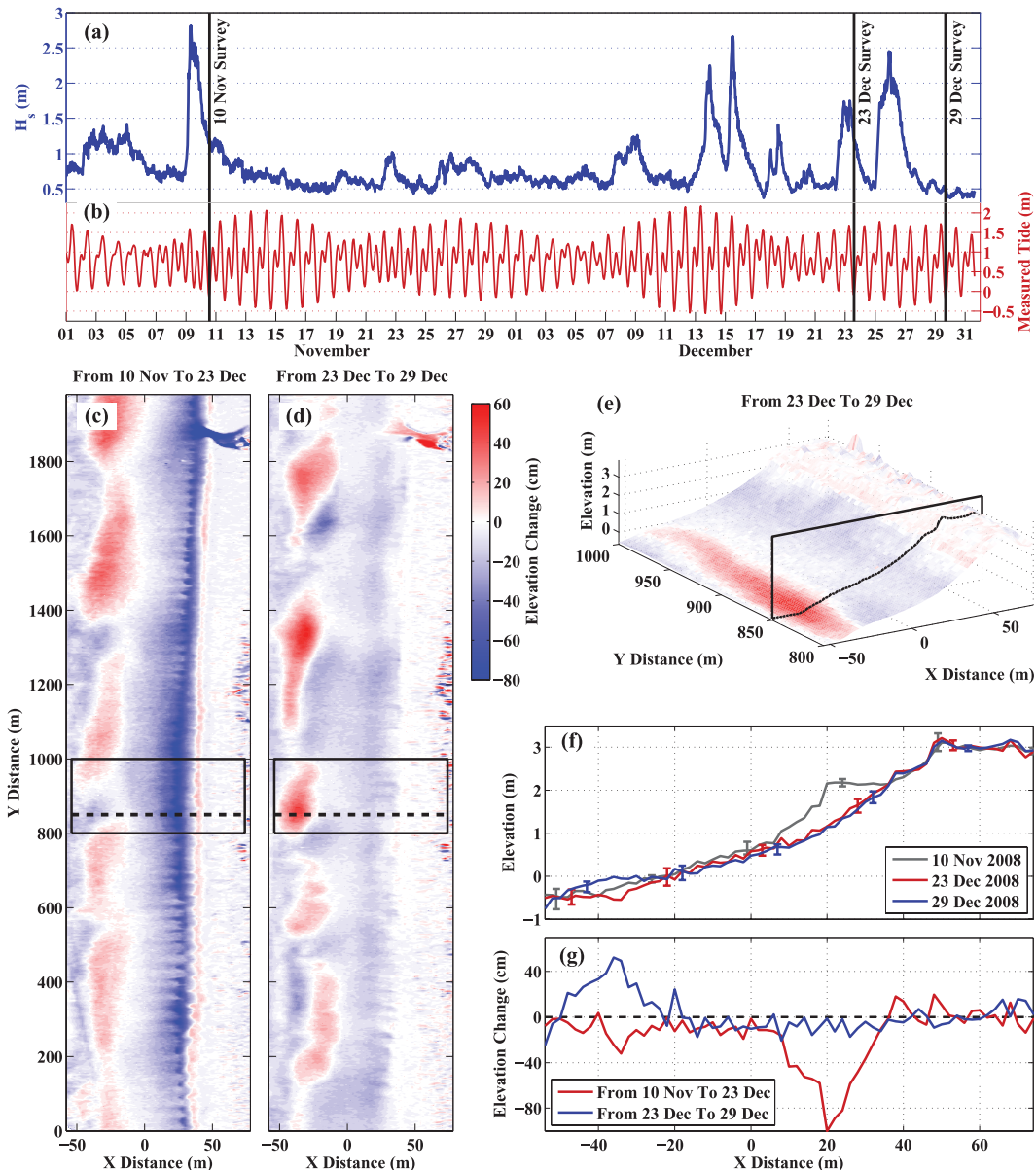


FIG. 9. Beach elevation evolution on a segment of beach in Camp Pendleton Marine Corps Base, flights conducted 10 Nov and 23 and 29 Dec 2008 with at least five passes each day: (a) Significant wave height ( $H_s$ ). (b) Measured water level. (c) The elevation change between 10 Nov and 23 Dec. (d) The elevation change between 23 and 29 Dec. (e) 3D view of the section outlined in (d). Red (blue) indicates elevation increase (decrease). For difference calculations, data from each day have been regridded to a  $2 \text{ m} \times 2 \text{ m}$  grid. (f) The transect marked in (e) and the dashed lines in (c) and (d). Points within 2 m of the transect are linearly interpolated, and error bars show two standard deviations from the mean. (g) The difference between the transects shown in (f). Coordinates have been rotated into cross- and alongshore components. The vertical reference is the North American Vertical Datum of 1988 (NAVD88), and all dates are in Pacific Standard Time.

passenger ferry, as it crossed the San Pedro Channel from Catalina Island to Long Beach, California. Wind speed at the time of the survey was  $4.1 \text{ m s}^{-1}$ , as measured by NDBC Station 46025, located 80 km to the east, and  $H_s$  was 0.7 m, as measured with the airborne lidar. The ship wake is visible in the lidar data up to 600 m behind the

vessel. Elevation measurements from one pass are shown in Fig. 11, where the bow wake, rooster tail, and background wave field are discernible. There is also evidence of sea spray in the lidar data several meters above the wake. Data are not corrected for the Doppler shift between the plane and ship wake.

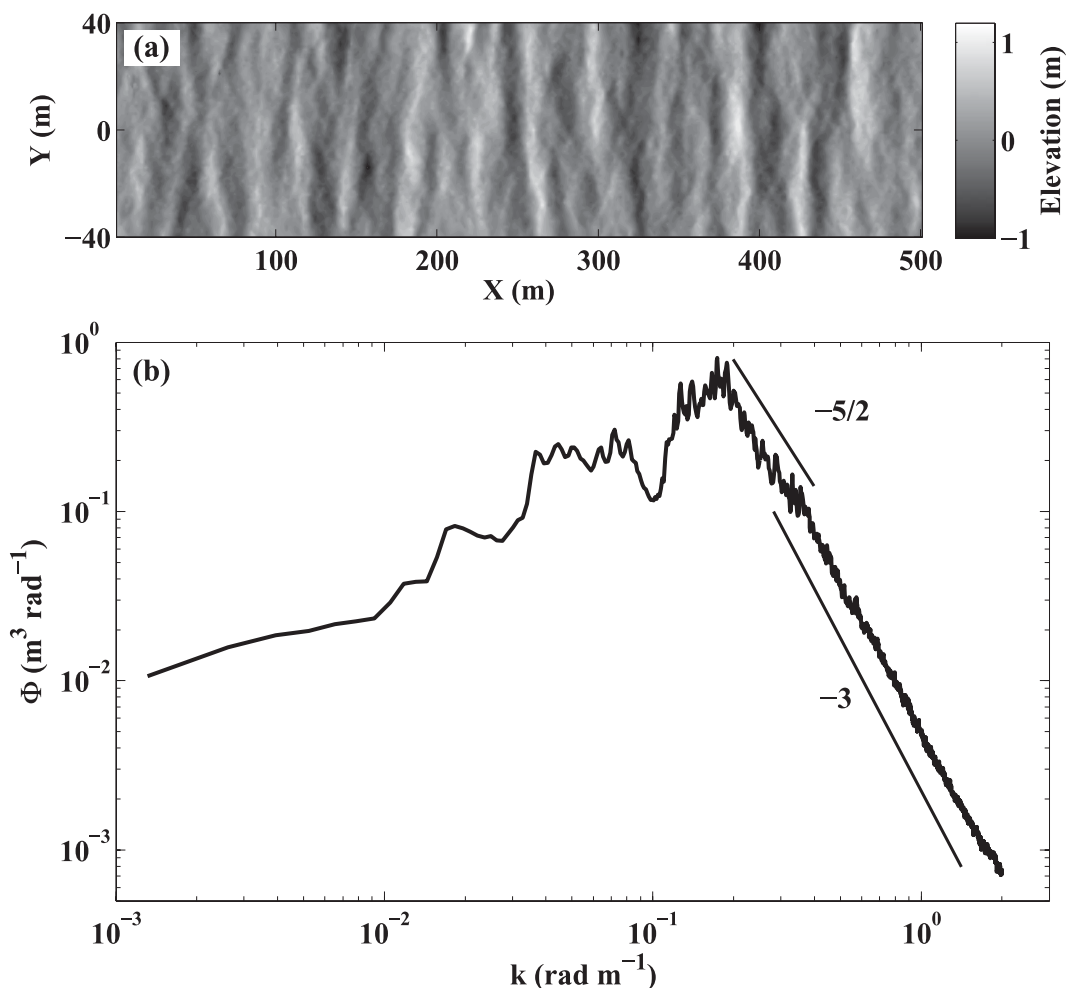


FIG. 10. (a) Typical sea surface topography data collected by the airborne lidar on 19 Sep 2008 during the ONR RaDyO experiment in the Santa Barbara Channel. Axes are not of equal scale. (b) The corresponding omnidirectional wavenumber spectrum. A  $10 \text{ km} \times 80 \text{ m}$  area is used in the spectral calculation.

Ocean wave data from our system have been successfully used to calibrate and test the data from an X-band Wave and Surface Current Monitoring System (WaMoS, <http://www.oceanwaves.org/>) station (E. J. Terrill 2009, personal communication). WaMoS uses marine radar to infer sea and swell state, and currently the inversion of radar backscatter to wave and current information requires site-specific calibration. Airborne lidar provides an accurate high-resolution ground truth for WaMoS calibration.

### c. Coral reef monitoring

The airborne lidar system was installed in a Cessna Caravan and used to survey the reef and ocean surrounding Lady Elliot Island in the Great Barrier Reef in April 2008. The surveys were part of a larger project designed to measure large- and small-scale processes (currents, waves, and turbulence) in the coral reef sys-

tem and to quantify the surface-wave energy fluxes and mixing in the reef lagoon. A composite elevation map of the island and lagoon from one afternoon of surveying on 6 April 2008 at spring low tide is shown in Fig. 12.

A variety of in situ instrumentation measured tides, waves, and water variables (temperature, salinity, dissolved  $\text{O}_2$ , and pH) inside and outside the lagoon. A meteorological station in the lagoon measured upwelling and downwelling radiation, temperature, and humidity, and included an eddy-covariance system to measure momentum,  $\text{CO}_2$ , heat, and water vapor fluxes. With the airborne lidar system, we measured the wave field around the island and in the lagoon, with the goal of testing the practicality of using airborne measurements to obtain wave energy fluxes incident on a reef and lagoon system.

The one-dimensional wave energy flux spectrum  $F(k_1)$  is approximated by

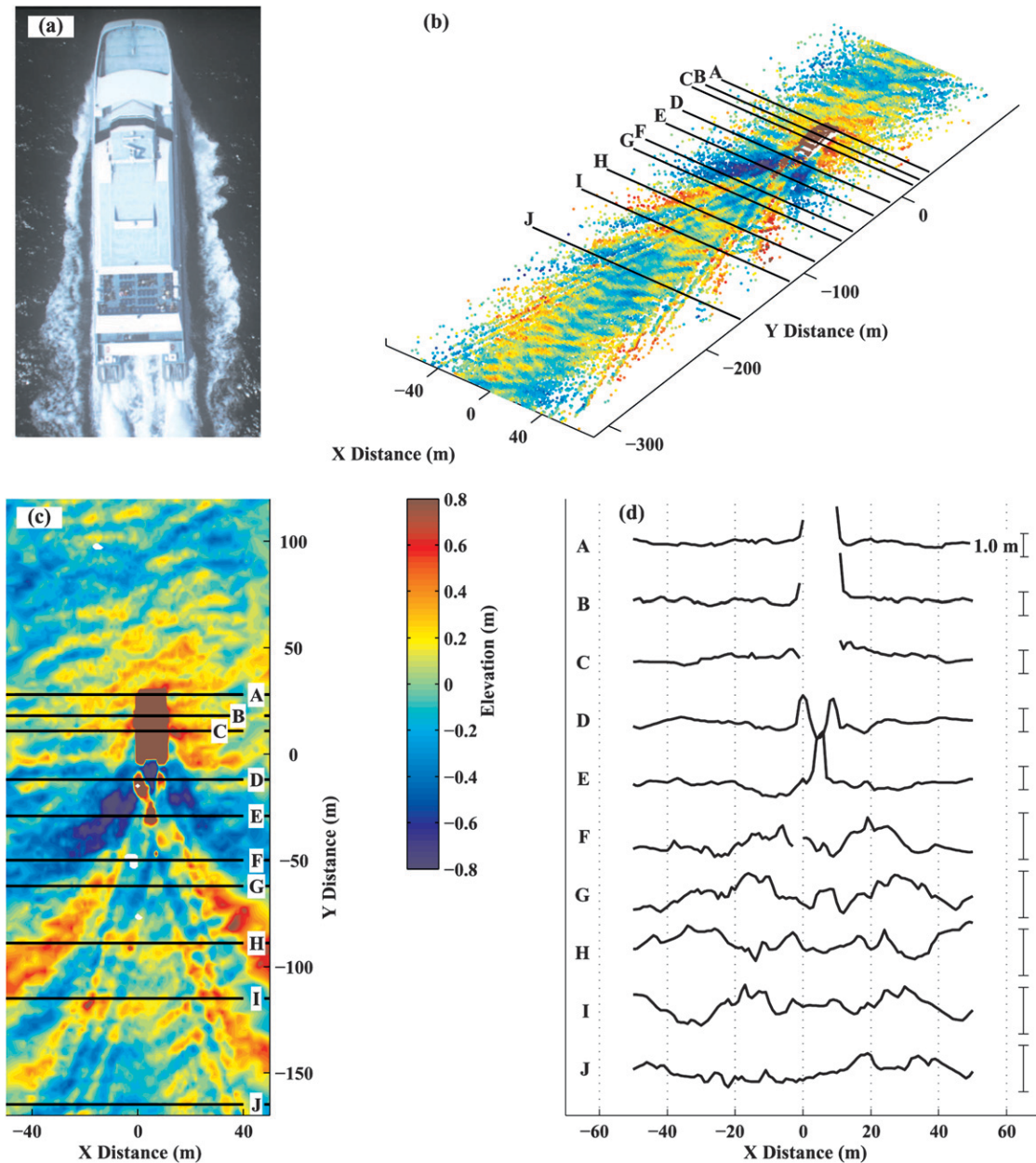


FIG. 11. Wake of a 44-m catamaran ferry measured by the airborne lidar system. Aircraft altitude is 150 m, speed  $58 \text{ m s}^{-1}$ . The vessel's speed is  $11 \text{ m s}^{-1}$ , opposing the aircraft flight direction. The profiles of sections A–J, marked in (b) and (c) are shown in (d). The bow wake is distinguishable in sections B and C; the rooster tail in E.

$$F(k_1) = E(k_1)c_{g1}(k_1). \quad (3)$$

In (3)  $E(k_1)$  is the estimated one-dimensional wave energy spectrum, such that

$$\int E(k_1) dk_1 = \frac{1}{2} \rho g a^2, \quad (4)$$

where  $k_1$  is the along-flight wavenumber,  $\rho$  is the density of seawater,  $g$  the acceleration due to gravity, and  $a^2$  the mean-squared wave amplitude. The group velocity is  $c_{g1} = \partial\omega/\partial k_1$ , where  $\omega$  is the angular frequency related to  $k_1$  and depth  $h$ , assuming the linear dispersion relationship,  $\omega^2 = gk_1 \tanh(k_1 h)$ . With bathymetric maps for  $h$  and the wavenumber spectra measured by the lidar, the wave energy flux can be calculated locally.



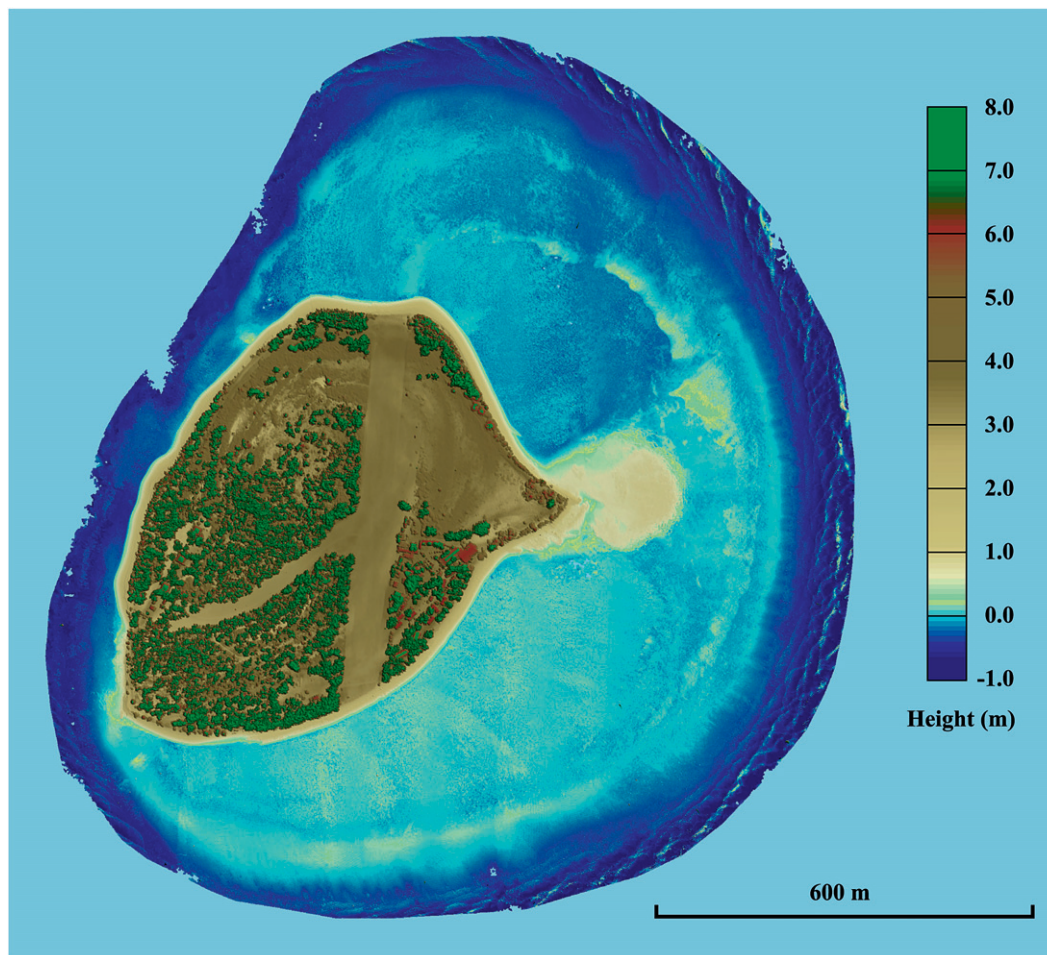


FIG. 12. Lady Elliot Island, Great Barrier Reef, Australia (24.11°S, 152.72°E): composite elevation map of one afternoon of airborne lidar surveys at spring low tide. The grass strip runway, trees and buildings, waves breaking on the rim, and exposed coral features are all visible.

Figure 13 shows sample transects of airborne lidar data from high and low tide surveys and one-dimensional wavenumber spectra of wave energy flux, illustrating the large change in wave energy over the reef rim. Group velocity is calculated assuming constant depths for each area. Wave energy flux decreases by over 90% for wavenumbers less than  $0.38 \text{ rad m}^{-1}$  ( $\lambda > 16.5 \text{ m}$ ). The energy lost from the wave field feeds into currents and wave setup or is dissipated by breaking and bottom friction (Lowe et al. 2005).

Manual GPS surveys inside the lagoon with a Leica Geosystems GPS System 1200 captured the reef and sand bottom bathymetry at approximately 1-m spacing along each transect. Eight manual surveys measured the southern lagoon and rim, with a section of one survey shown in Fig. 14. At low tide, when the larger coral heads are exposed, airborne lidar surveys are in good agreement with the manual surveys (<10-cm rms difference for exposed targets).

#### d. Mt. Soledad landslide

In previous studies, airborne lidar surveys have been conducted for the purposes of historic landslide mapping (Schulz 2007; McKean and Roering 2004) and for recent landslide detection (Ardizzone et al. 2007; Corsini et al. 2007).

Two flights with the present system documented the aftermath of a landslide on Mount Soledad in La Jolla, California, which occurred on 3 October 2007. The landslide destroyed three homes, left eight others uninhabitable, and led to the proclamation of a state of emergency by the governor of California (Vigil 2008).

Surveys were conducted on 4 and 5 October, the two days following the event, at altitudes from 270 to 300 m AGL. The point density from eight passes is  $6 \text{ m}^{-2}$ . Linearly interpolated elevation data from the 5 October survey and a composite image from the 3CCD camera are shown in Fig. 15. A 2-m drop in the road elevation is



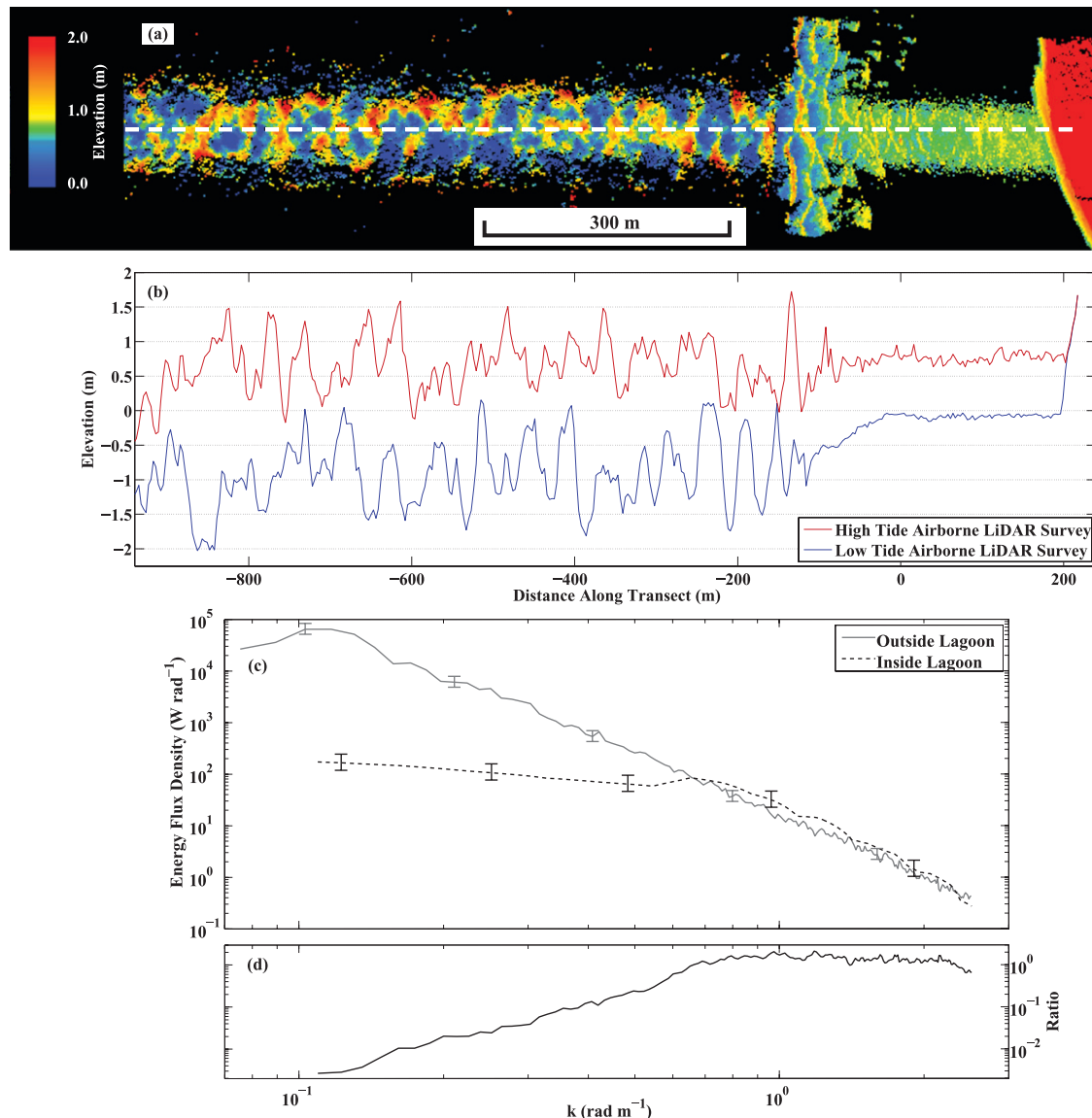


FIG. 13. Sample airborne lidar data from high tide and low tide surveys at Lady Elliot Island in April 2008. (a) Elevation map from one pass of a high tide survey. Waves are propagating from left to right, breaking on the rim, and continuing through the lagoon toward the island. The higher reflectivity of foam from waves breaking over the rim results in a notably larger swath width there. (b) Profile of the transect marked by the white dashed line in (a) at high tide (red) compared with the profile of the same transect from a low tide survey (blue). The structures seen inside the lagoon at low tide are exposed coral. (c) Sample 1D wavenumber spectra of wave energy flux, corresponding to measurements from inside and outside the lagoon from the same high tide survey shown in (a). Eleven 2-km transects are used for the spectral calculation outside the lagoon, and six 200-m transects are used for inside. Error bars indicate 95% confidence intervals. (d) The ratio of the energy flux inside the lagoon to outside.

evident, as well as lateral movement of the sidewalk of up to 5 m.

## 5. Discussion

We have demonstrated the utility for ocean and coastal research of a low-cost, portable, platform-independent airborne scanning lidar system based on the Riegl LMS-

Q240i lidar and a CodaOctopus F180+ GPS/INS system. We have measured its performance and investigated possible research applications with multiple flights over the coastal environments of southern California aboard a Piper Twin Comanche and of Lady Elliot Island in the Great Barrier Reef aboard a Cessna Caravan.

Acquisition, calibration, and postprocessing routines were developed in house. The eye-safe rating of this

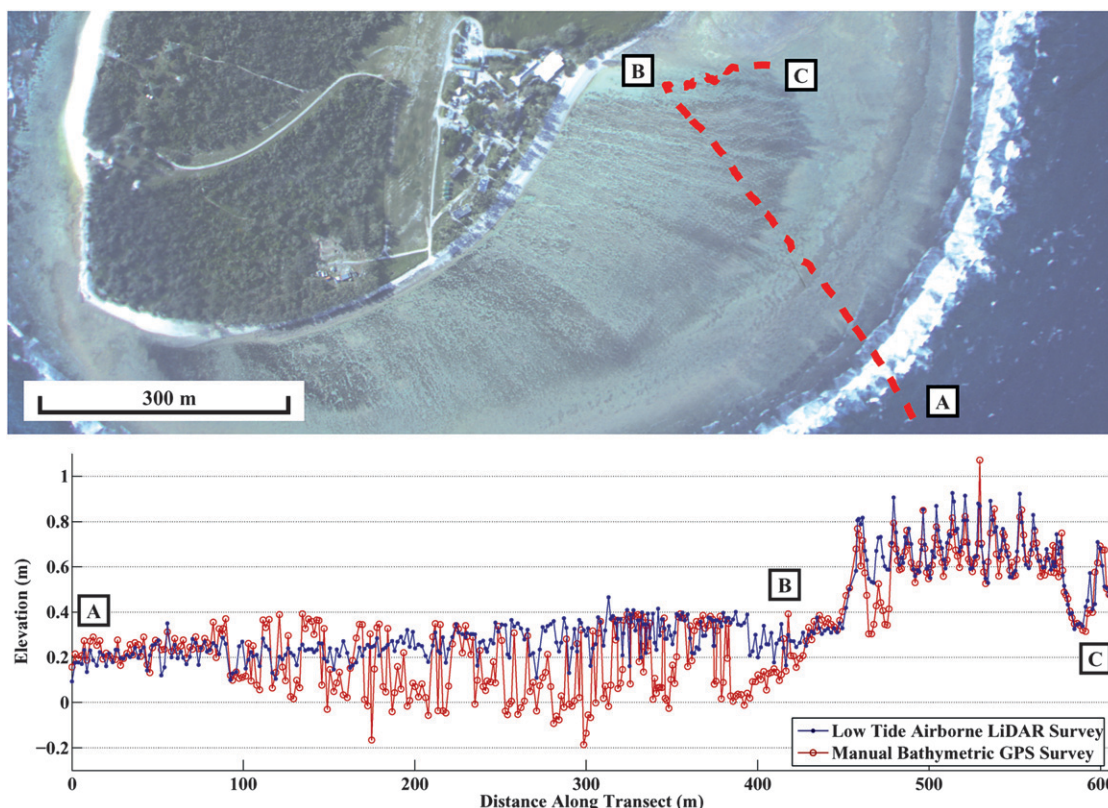


FIG. 14. Comparison of airborne lidar survey at low tide (blue) with a manual bathymetric GPS transect (red). The transect marked with a dashed red line (top panel) is shown in the lower panel. The transect starts on the exposed island rim (A), traverses the lagoon (A–B), and ends on a dry section of reef (B–C). The bathymetric survey captures the underlying reef structure, including the radial channel features visible in the top panel, which is a composite of several images from the 3CCD camera.

lidar permits the system to be flown at low altitudes, thereby increasing point density and decreasing the effects of attitude error. Point density as a function of cross-swath distance and flight altitude has been quantified, providing a useful tool for future mission planning. Resolution could be enhanced with a lidar unit having a higher pulse repetition rate.

We have successfully used the airborne lidar system to measure beach erosion and accretion caused by several moderate winter storm events at Camp Pendleton Marine Corps Base. The portable system design allows for a fast response to such events, well within the limit of wave forecasting. Since the system can resolve the peak accretion and erosion states that come just before and after storm events, it can aid in improving cross- and alongshore beach erosion models (M. L. Yates 2009, personal communication).

With a flight altitude of 120 m and ground speed of  $53 \text{ m s}^{-1}$ , point density over the ocean is high enough to resolve wavelengths  $\lambda \geq 3.8 \text{ m}$ . We are able to clearly resolve equilibrium omnidirectional wavenumber spec-

tra ( $k^{-5/2}$ ), saturation spectra ( $k^{-3}$ ), and the boundary between them in airborne lidar wave data from the Santa Barbara Channel.

The airborne lidar system has potential for measurements of ship wakes and for other full-scale ship hydrodynamic and sea-keeping studies, complementing vessel-based incident wave and wake studies (Terrill and Fu 2008). It is now well known that the wakes of surface vessels can persist for many kilometers behind the vessel. The system can be used to study the wave environment in which a vessel is operating and the evolution of the wake from the near to the far field.

In a related study, we have demonstrated the use of this airborne lidar system for in situ calibration of marine-radar-based measurements of ocean surface waves. Such systems (e.g., WaMoS) use the modulation of the radar backscatter by the waves to infer their speed and height. While the former measurement is straightforward, the latter is not and depends on a number of phenomena. Airborne lidar is perhaps the only way to provide accurate spatiotemporal measurements of

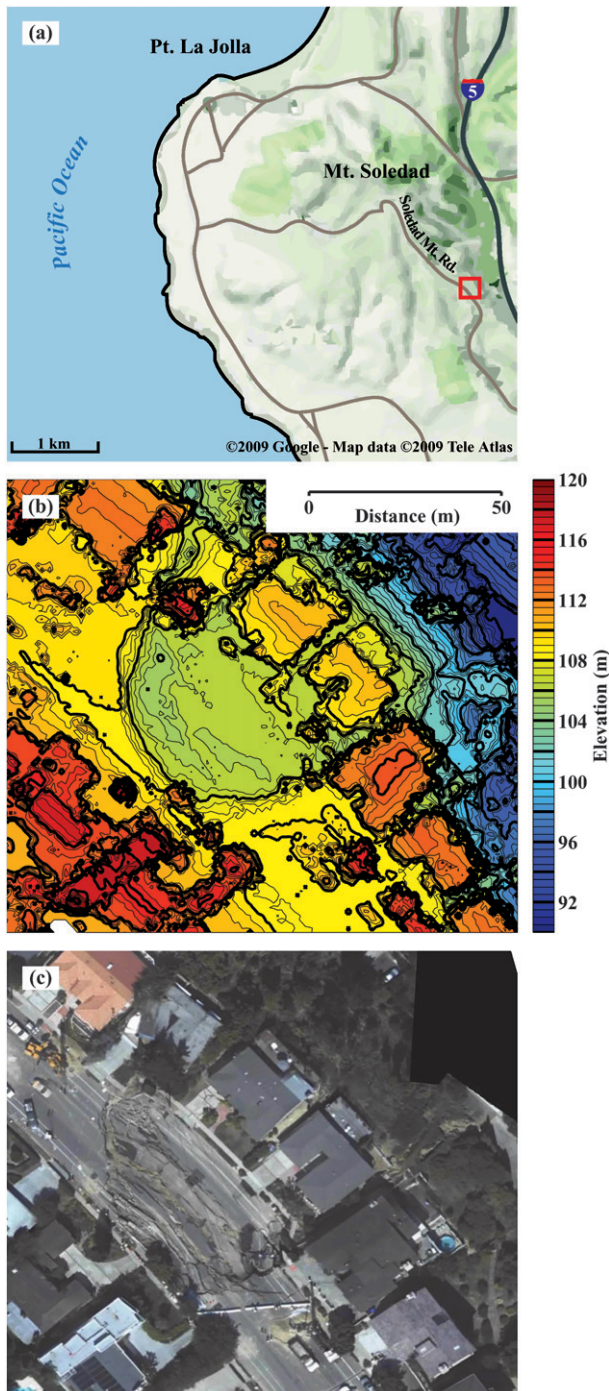


FIG. 15. Landslide on Mt. Soledad, La Jolla, (32.8246°N, 117.2364°W) in October 2007: (a) Map highlighting the area shown in (b),(c) with a red box; downtown San Diego is located 15 km to the south. (b) A composite elevation map from eight passes over the affected area. Bold contours are at 2.0-m intervals, fine at 0.5 m. (c) A composite image generated with frames from the 3CCD camera.

waves for the calibration of the radar for wave measurements.

We installed the airborne lidar system on a second aircraft and incorporated it into an experiment within the Great Barrier Reef, where we explored the feasibility of monitoring coral reef environments using airborne measurements. With the airborne lidar, we mapped the island topography, lagoon, coral heads, and surrounding wave field of Lady Elliot Island. A suite of in situ instrumentation measured waves, currents, turbulence, and water properties inside and outside the lagoon. Future analysis will further quantify the wave energy flux and energy dissipation due to breaking and bottom friction. The correlation of airborne measurements with in situ observations has many applications for large-scale, long-term studies in the monitoring of coral reef environments.

The portable, integrated system also permits a rapid response for the topographic mapping of natural disasters, as demonstrated by our ability to map a local landslide within 30 h of the event.

The vertical rms error of the current system is comparable to error levels achieved by more expensive turnkey commercial lidar systems available for airborne applications. At a fraction of the cost, this system is attractive for a wide variety of research applications. As lidar and GPS/INS systems become cheaper and more widely available, we expect airborne lidar will become a more common tool for geophysical and oceanographic research.

**Acknowledgments.** This work was supported by grants to WKM from the National Science Foundation (OCE 02-42083), the Office of Naval Research (N00014-06-1-0048, RaDyO DRI; N00014-08-1-0499, Hi-Res DRI), and a contract from NAVSEA (MAC N00024-01-D-7017, S6040010). Eric Terrill generously lent us the F180+. The Lady Elliot Island experiment was conducted in collaboration with Jason Middleton and Moninya Roughan at the University of NSW with support from the Australian Research Council Discovery Projects DP0771055. We thank Peter Gash, Wayne Fox, the pilots with Seair, and the LEI staff who made the surveys in the GBR possible. Manual GPS surveys in LEI were conducted by Nick Statom. Ryan McCabe provided bathymetry data surrounding LEI, and Leonel Romero aided in spectral analysis. BDR was funded in part by a Jacobs Fellowship and grants from the California Space Grant Consortium at UCSD.

## REFERENCES

- Ardizzone, F., M. Cardinali, M. Galli, F. Guzzetti, and P. Reichenbach, 2007: Identification and mapping of recent rainfall-induced landslides using elevation data collected by airborne lidar. *Nat. Hazards Earth Syst. Sci.*, **7**, 637–650.



- Badulin, S. I., A. N. Pushkarev, D. Resio, and V. E. Zakharov, 2005: Self-similarity of wind-driven seas. *Nonlinear Processes Geophys.*, **12**, 891–945.
- Brock, J. C., C. W. Wright, A. H. Sallenger, W. B. Krabill, and R. N. Swift, 2002: Basis and methods of NASA Airborne Topographic Mapper lidar surveys for coastal studies. *J. Coastal Res.*, **18**, 1–13.
- Corsini, A., L. Borgatti, F. Coren, and M. Vellico, 2007: Use of multitemporal airborne lidar surveys to analyse post-failure behaviour of earth slides. *Can. J. Remote Sens.*, **33**, 116–120.
- Dysthe, K. B., K. Trulsen, H. E. Krogstad, and H. Socquet-Juglar, 2003: Evolution of a narrow-band spectrum of random surface gravity waves. *J. Fluid Mech.*, **478**, 1–10.
- Filin, S., 2003: Recovery of systematic biases in laser altimetry data using natural surfaces. *Photogramm. Eng. Remote Sens.*, **69**, 1235–1242.
- Forsberg, R., K. Keller, and S. M. Jacobsen, 2001: Laser monitoring of ice elevations and sea-ice thickness in Greenland. *Int. Arch. Photogramm. Remote Sens.*, **34**, 163–168.
- Hwang, P. A., D. W. Wang, E. J. Walsh, W. B. Krabill, and R. N. Swift, 2000: Airborne measurements of the wavenumber spectra of ocean surface waves. Part I: Spectral slope and dimensionless spectral coefficient. *J. Phys. Oceanogr.*, **30**, 2754–2767.
- Katzenbeisser, I. R., 2003: About the calibration of lidar sensors. *Proc. ISPRS Workshop 3-D Reconstruction from Airborne Laser-Scanner and InSAR Data*, Dresden, Germany, ISPRS. [Available online at [http://www.isprs.org/commission3/wg3/workshop\\_laserscanning/papers/Katzenbeisser\\_ALSDD2003.pdf](http://www.isprs.org/commission3/wg3/workshop_laserscanning/papers/Katzenbeisser_ALSDD2003.pdf).]
- Keller, K., G. Casassa, A. Rivera, R. Forsberg, and N. Gundestrup, 2007: Airborne laser altimetry survey of Glacier Tyndall, Patagonia. *Global Planet. Change*, **59**, 101–109.
- Lowe, R. J., J. L. Falter, M. D. Bandet, G. Pawlak, M. J. Atkinson, S. G. Monismith, and J. R. Koseff, 2005: Spectral wave dissipation over a barrier reef. *J. Geophys. Res.*, **110**, C04001, doi:10.1029/2004JC002711.
- McKean, J., and J. Roering, 2004: Objective landslide detection and surface morphology mapping using high-resolution airborne laser altimetry. *Geomorphology*, **57**, 331–351.
- Melville, W. K., L. Romero, and J. M. Kleiss, 2005: Extreme wave events in the Gulf of Tehuantepec. *Rogue Waves: Proc. 14th 'Aha Huliko 'a Hawaiian Winter Workshop*, Honolulu, HI, University of Hawaii at Manoa, 23–28.
- Meredith, A. W., D. Eslinger, and D. Aurin, 1999: An evaluation of hurricane-induced erosion along the North Carolina coast using airborne LIDAR surveys. NOAA Coastal Services Center Tech. Rep. NOAA/CSC/99031-PUB/001, 35 pp.
- Mohamed, A. H., and K. P. Schwarz, 1999: Adaptive Kalman filtering for INS/GPS. *J. Geod.*, **73**, 193–203.
- Onorato, M., A. R. Osborne, M. Serio, D. Resio, A. Pushkarev, V. E. Zakharov, and C. Brandini, 2002: Freely decaying weak turbulence for sea surface gravity waves. *Phys. Rev. Lett.*, **89**, 144501, doi:10.1103/PhysRevLett.89.144501.
- Phillips, O., 1985: Spectral and statistical properties of the equilibrium range in wind-generated gravity waves. *J. Fluid Mech.*, **156**, 505–531.
- Robertson, W., K. Zhang, and D. Whitman, 2007: Hurricane-induced beach change derived from airborne laser measurements near Panama City, Florida. *Mar. Geol.*, **237**, 793–801.
- Romero, L., and W. K. Melville, 2010a: Airborne observations of fetch-limited waves in the Gulf of Tehuantepec. *J. Phys. Oceanogr.*, in press.
- , and —, 2010b: Numerical modeling of fetch-limited waves in the Gulf of Tehuantepec. *J. Phys. Oceanogr.*, in press.
- Sallenger, A. H., W. Krabill, J. Brock, R. Swift, S. Manizade, and H. Stockdon, 2002: Sea-cliff erosion as a function of beach changes and extreme wave runup during the 1997–1998 El Niño. *Mar. Geol.*, **187**, 279–297.
- , and Coauthors, 2003: Evaluation of airborne topographic lidar for quantifying beach changes. *J. Coastal Res.*, **19**, 125–133.
- , H. F. Stockdon, L. Fauver, M. Hansen, D. Thompson, C. W. Wright, and J. Lillycrop, 2006: Hurricanes 2004: An overview of their characteristics and coastal change. *Estuaries Coasts*, **29**, 880–888.
- Schenk, T., 2001: Modeling and analyzing systematic errors in airborne laser scanners. Tech. Notes in Photogrammetry 19, the Ohio State University, 46 pp.
- Schulz, W. H., 2007: Landslide susceptibility revealed by lidar imagery and historical records, Seattle, Washington. *Eng. Geol.*, **89**, 67–87.
- Skaloud, J., and D. Lichti, 2006: Rigorous approach to bore-sight self-calibration in airborne laser scanning. *ISPRS J. Photogram. Remote Sens.*, **61**, 47–59.
- Stockdon, H., A. Sallenger, J. List, and R. Holman, 2002: Estimation of shoreline position and change using airborne topographic lidar data. *J. Coastal Res.*, **18**, 502–513.
- Terrill, E. J., and T. Fu, 2008: At-sea measurements for ship hydrodynamics. *Proc. 27th Symp. on Naval Hydrodynamics*, Seoul, South Korea, Office of Naval Research, 1–28.
- Vigil, J., 2008: Road finally opens year after landslide. *The San Diego Union Tribune*, 17 Oct. [Available online at [http://www.signonsandiego.com/uniontrib/20081017/news\\_1m17soledad1.html](http://www.signonsandiego.com/uniontrib/20081017/news_1m17soledad1.html).]
- Walsh, E. J., D. W. Hancock, D. E. Hines, R. N. Swift, and J. F. Scott, 1985: Directional wave spectra measured with the surface contour radar. *J. Phys. Oceanogr.*, **15**, 566–592.
- Woolard, J. W., and J. D. Colby, 2002: Spatial characterization, resolution, and volumetric change of coastal dunes using airborne lidar Cape Hatteras, North Carolina. *Geomorphology*, **48**, 269–287.
- Yates, M. L., 2009: Seasonal sand level changes on Southern California beaches. Ph.D. thesis, University of California, San Diego, 155 pp.
- , R. Guza, R. Gutierrez, and R. Seymour, 2008: A technique for eliminating water returns from lidar beach elevation surveys. *J. Atmos. Oceanic Technol.*, **25**, 1671–1682.
- Young, A., and S. Ashford, 2006: Application of airborne lidar for seacliff volumetric change and beach-sediment budget contributions. *J. Coastal Res.*, **22**, 307–318.

Copyright of Journal of Atmospheric & Oceanic Technology is the property of American Meteorological Society and its content may not be copied or emailed to multiple sites or posted to a listserv without the copyright holder's express written permission. However, users may print, download, or email articles for individual use.